ACS SENSORS

pubs.acs.org/acssensors Article

Shaped Magnetogel Microparticles for Multispectral Magnetic Resonance Contrast and Sensing

Samuel D. Oberdick,* Stephen J. Dodd, Alan P. Koretsky, and Gary Zabow*

Cite This: *ACS Sens.* 2024, 9, 42−51 Read Online

ABSTRACT: Multispectral magnetic resonance imaging (MRI) contrast agents are microfabricated three-dimensional magnetic structures that encode nearby water protons with discrete frequencies. The agents have a unique radiofrequency (RF) resonance that can be tuned by engineering the geometric parameters of these microstructures. Multispectral contrast agents can be used as sensors by incorporating a stimulus-driven shape-changing response into their structure. These geometrically encoded magnetic sensors (GEMS) enable MRI-based sensing via environmentally induced changes to their geometry and their corresponding RF resonance. Previously, GEMS have been made using thin-film lithography techniques in a cleanroom environment. While these approaches offer precise control of the microstructure, they can be a limitation for researchers who do not have cleanroom access or microfabrication expertise. Here, an alternative approach for GEMS fabrication based on soft lithography is introduced. The fabrication scheme uses cheap, accessible materials and simple chemistry to produce shaped magnetic hydrogel microparticles with multispectral MRI contrast properties. The microparticles can be used as sensors by fabricating them out of shape-reconfigurable, "smart" hydrogels. The change in shape causes a corresponding shift in the resonance of the GEMS, producing an MRI-addressable readout of the microenvironment. Proof-of-principle experiments showing a multispectral response to pH change with cylindrical shell-shaped magnetogel GEMS are presented.

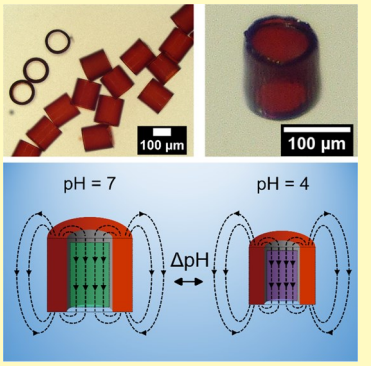

KEYWORDS: *magnetic resonance imaging, soft lithography, hydrogel microparticles, contrast agents, smart sensing*

Advances in engineering at the micro- and nanoscale have led to the development of miniaturized biosensors with increasing complexity and functionality.[1] This is especially true in the field of biomedical imaging, where micro- and nanoparticles with surface-engineered specificity, tailored nanomaterial properties, bioresponsive sensing capabilities, and "smart" contrast mechanisms have been created to address questions in clinical and biological research.[2−5] Increased functionality for nano- and microsensors enables researchers to interrogate biosystems in new ways on increasingly small scales. However, increased functionality often requires considerable engineering at the nano- or microscale, which may necessitate niche expertise or costly infrastructure. This can be a hurdle to researchers who want to create advanced imaging agents in their own lab or industrial manufacturers who are interested in scalable, parallelized manufacturing processes for biosensors. As such, there is inherent value in exploring alternative fabrication schemes for advanced imaging agents that reduce either the cost or infrastructure while retaining critical functional properties.

This article describes a new fabrication scheme for producing multispectral magnetic resonance imaging (MRI) contrast agents based on physical changes in magnetic microstructures. The new method maintains key properties for contrast generation while also reducing the time, cost, and infrastructure needed for device production. Multispectral contrast agents are an emerging form of contrast agent that operate via localized magnetic field control with microengineered three-dimensional architectures.[6−8] As opposed to other approaches that multiplex agents based on chemical shift, the geometry of these contrast agents encodes surrounding water protons with a unique radiofrequency (RF) resonance, which can be probed using nuclear magnetic resonance (NMR). The RF frequency associated with the contrast agents can be tuned via geometric properties of the microstructures, thereby associating distinct frequencies, or "colors," with specific architectures. These agents offer advantages over traditional MRI contrast agents. For example, the RF "color" signature of the microparticles is shifted far from the biochemical background spectrum and standard NMR chemical shifts, providing a pathway for the unambiguous localization and detection of contrast agents. The contrast agents can also be used as geometrically encoded magnetic sensors (GEMS) by engineering geometric characteristics that

Received: July 6, 2023
Revised: October 30, 2023
Accepted: December 1, 2023
Published: December 19, 2023

https://doi.org/10.1021/acssensors.3c01373
ACS Sens. 2024, 9, 42−51

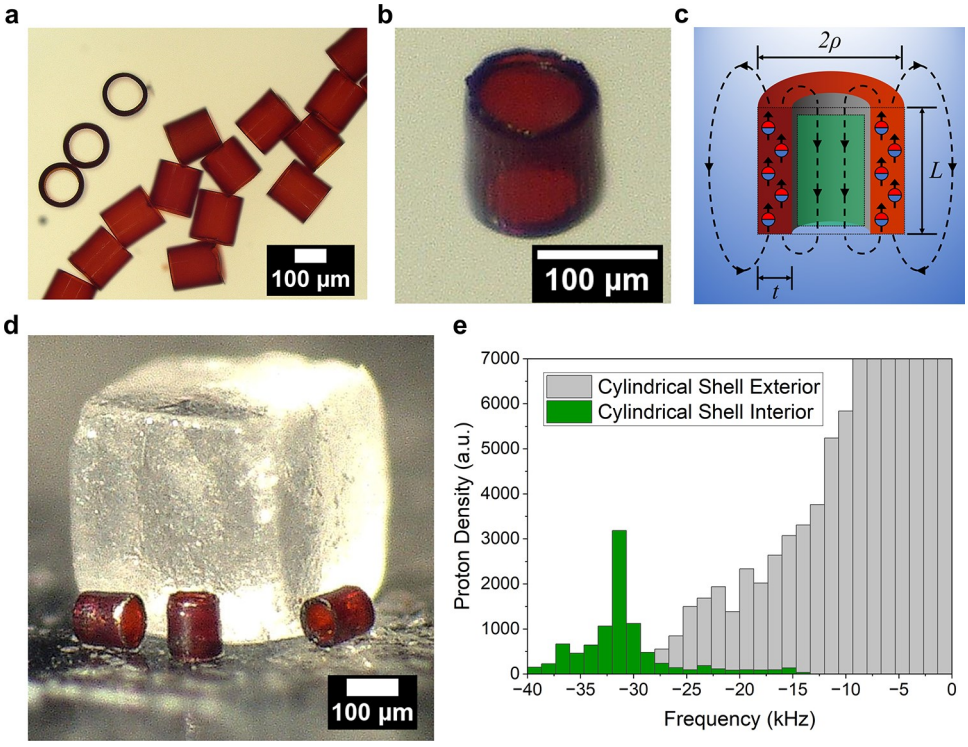

Figure 1. (a) Optical image of cylindrical shell microparticles immersed in pH 7 buffer solution. (b) Optical image of a single geometrically encoded magnetic sensor (GEMS) sitting on a dry surface. (c) Cartoon schematic showing magnetization profile of magnetogel GEMS and green shaded interior region highlighting the region where multispectral contrast is generated. (d) Several GEMS displayed next to a grain of salt (NaCl). (e) Calculation of the Larmor frequency for protons contained within the cylindrical shell and, also, exterior to the cylindrical shell.

change in response to environmental stimuli.[9] The advanced three-dimensional shapes of these contrast agents have been previously produced through microfabrication in a cleanroom environment using lithographic techniques adapted from thin-film engineering.[6−12] While these procedures create contrast agents with exquisite functionality, the fabrication is costly and infrastructure-intensive. It also requires substantial micro-fabrication expertise. Herein, an alternative approach for the fabrication of GEMS is described. The approach uses soft lithography techniques and simple chemical functionalization to produce GEMS with multispectral contrast properties and biosensing capabilities.

The fabrication procedure described here uses soft lithography-based micromolding techniques and produces GEMS made from a magnetic hydrogel, or magnetogel, composite. The magnetogel microparticles have a hollow cylinder shape, which is used to generate multispectral MRI contrast. The shaped microparticles are fabricated in three steps. First, an accurate mold, or master template, is created out of a silicon wafer using photolithography and reactive ion etching. Second, soft lithography uses this template to produce shaped microparticles made from a poly(ethylene glycol) (PEG)-based hydrogel. Third, in situ coprecipitation is used to grow magnetic iron oxide nanoparticles within the hydrogel network of the microparticles. The final structures have the necessary shape and magnetic properties for the generation of multispectral contrast and show NMR frequency offsets on the order of several tens of kHz when magnetized by an MRI scanner. Detection of a single 100-μm-scale magnetogel microparticle is described. Sensing capabilities are also presented, whereby the shape-changing response of a smart hydrogel is used to transduce changes in environmental pH into MRI-interrogable changes in the RF offset frequency.

MICROPARTICLE STRUCTURE AND MULTISPECTRAL CONTRAST

The multispectral MRI contrast of the microparticles arises from a combination of their cylindrical shell geometry and the material properties. The microparticles are made of a hydrogel-magnetic nanoparticle composite, composed of a cross-linked poly(ethylene glycol diacrylate) (PEGDA) and acrylic acid (AA) hydrogel filled with iron oxide nanoparticle inclusions. The iron oxide nanoparticles are magnetite (Fe_3O_4) and have a diameter of approximately 5 nm (Supporting Information). Iron oxide nanoparticles were chosen because of their relatively high magnetization and intrinsic biocompatibility. Throughout the manuscript, the iron oxide nanoparticles will be referred to as superparamagnetic iron oxide nanoparticles, or SPIONs, so as not to confuse them with the relatively larger, yet also still small, GEMS microparticles themselves. Figure 1a shows the microparticles submerged in a pH 7 buffer solution. The red color of the microparticles comes from the SPIONs that are integrated throughout the hydrogel network. Figure 1b shows a dry microparticle sitting on a surface. The angle of the image displays the hollow cylinder structure of the microparticle. The dry magnetogel microparticles swell by a factor of 1.3× when placed in aqueous solution due to the water-absorbing properties of the PEGDA/AA hydrogel network. To give an impression of the size of microparticles used in this study, Figure 1d shows a microscope image of several GEMS placed next to a grain of salt.

The hollow cylinder shape of the GEMS can be used to produce tunable nuclear magnetic resonance (NMR) shifts of

https://doi.org/10.1021/acssensors.3c01373
ACS Sens. 2024, 9, 42−51

water contained within the interior of the microparticle.[7] When the GEMS are placed in a strong magnetic field, such as the one used for NMR or MRI, the field magnetizes the SPIONs embedded in the composite. The cylindrical shell shape of the GEMS allows the stray magnetic, or demagnetizing, fields of the embedded SPIONs to add together to form a region of uniform magnetic field within the shell. Figure 1c shows a schematic of this effect. During a ^{1}H NMR or MRI experiment, the Larmor frequency of protons is given by $f = \gamma B_0$, where γ is the gyromagnetic ratio of protons (42.577 MHz/T) and B_0 is the magnitude of the applied magnetic field. The field experienced by protons within the hollow cylinder is a superposition of the primary field of the MRI scanner, B_0, and the field generated by the GEMS. The field of the GEMS reduces the magnitude of the magnetic field within the cylinder, causing protons there to precess with a decreased frequency. The magnitude of the frequency offset is a function of the geometric and magnetic properties of the cylindrical shell and is given by

$$f_{\text{offset}} = \mu_0 \gamma \frac{m}{V} \left(\frac{L}{\sqrt{L^2 + (2\rho + t)^2}} - \frac{L}{\sqrt{L^2 + (2\rho - t)^2}} \right) \quad (1)$$

where μ_0 is the permeability of free space, m is the magnetic moment of the GEMS, V is the volume of the cylindrical shell, 2ρ is the cylinder diameter, t is the thickness of the shell, and L is the length.[7]

Magnetic simulations can be used to understand the magnetic properties of the GEMS. Figure 1e shows a histogram of Larmor frequencies, which are proportional to the magnetic fields calculated within a cylindrical shell and also outside of the shell. The material properties of the shell were chosen based on experimental measurements of the magnetogel GEMS (Supporting Information). The spectrum generated by the histogram shows a clear peak at −31 kHz for protons contained within the interior of the shell, corresponding to the amount by which the overall detected frequency of the protons is reduced from that of the background B_0 field.

In addition to multispectral MRI properties, the magnetogel GEMS were fabricated from hydrogel materials that exhibit a shape-changing, smart response to environmental pH. The hydrogels contract in an acidic environment and expand when placed in neutral or basic environments.

FABRICATION AND MAGNETIC PROPERTIES OF MICROPARTICLES

Microparticle Fabrication. The magnetogel GEMS microparticles were fabricated in two main steps. First, the shaped hydrogel microparticles were created with a soft lithography process using poly(dimethylsiloxane) (PDMS). The hydrogel microparticles were later filled with SPIONs by using in situ coprecipitation. Figure 2 describes the soft lithography process flow used in the first step. Soft lithography[13,14] was used because it can produce polymeric microparticles with engineerable shapes,[15−19] critical to the fabrication of the cylindrical shell geometry. The process is outlined in Figure 2a−f. First, uncured PDMS was poured on top of a silicon master mold and cured (Figure 2a). The fabrication of the master mold was the only part of the process performed in a dedicated cleanroom microfabrication environment. The mold had hollow cylinder features that were etched using a combination of photolithography and deep reactive ion

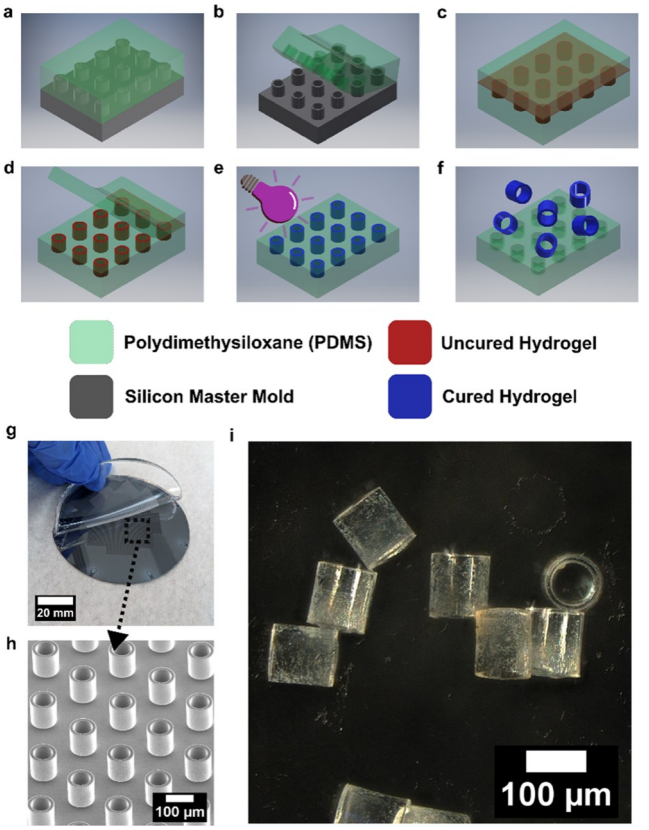

Figure 2. Process flow for soft lithography scheme displayed in (a)−(f). (a) A poly(dimethylsiloxane) (PDMS) mold (green) is cured on top of a silicon master mold (gray). (b) The PDMS mold is peeled away from the silicon. (c) The PDMS mold is filled with uncured hydrogel (red) and a flat piece of PDMS is placed on top of the molded surface to promote uniform filling of the precursor. The mold is also placed in a vacuum to pull the liquid hydrogel precursor into the recessed PDMS mold. (d) The flat PDMS is slowly removed leaving behind uncured hydrogel within the recessed regions of the elastomer mold. (e) The hydrogel is cured within the molds via exposure to ultraviolet light. (f) The cylindrical shell-shaped microparticles are removed from the mold through immersion in a basic solution (0.5 mol/L NaOH), which causes the microparticles to swell and push themselves out of the mold. (g) Optical image of a PDMS elastomer being peeled away from a 76.2 mm silicon wafer, which has been micropatterned with an array of cylindrical shell-shaped features. (h) Scanning electron microscopy (SEM) image of the patterned silicon surface. (i) Optical microscope image of microparticles after soft lithography process, dried on a flat surface.

etching (Figure 2g,h) and could be used repeatedly after being made. After the PDMS was cured, it was peeled away from the Si master mold (which is coated with an antiadhesion C_4F_8 passivation layer) creating a negative of the patterned Si mold (Figure 2b). The PDMS mold was then filled with a hydrogel precursor (2:1 mixture of PEGDA and acrylic acid) and covered with a separate flat piece of PDMS (Figure 2c). The PDMS/hydrogel precursor/PDMS stack was placed in a vacuum to pull the hydrogel precursor into the high-aspect-ratio molds. Then, the flat PDMS piece was slowly removed, drawing the hydrogel liquid layer across the molded surface and leaving hydrogel precursor loaded within the recessed cylindrical shell molds using discontinuous dewetting (Figure 2d).[20] The combination of pulling vacuum and discontinuous dewetting has been shown to be an effective way to produce large area arrays of shaped microparticles using PDMS-based

https://doi.org/10.1021/acssensors.3c01373
ACS Sens. 2024, 9, 42−51

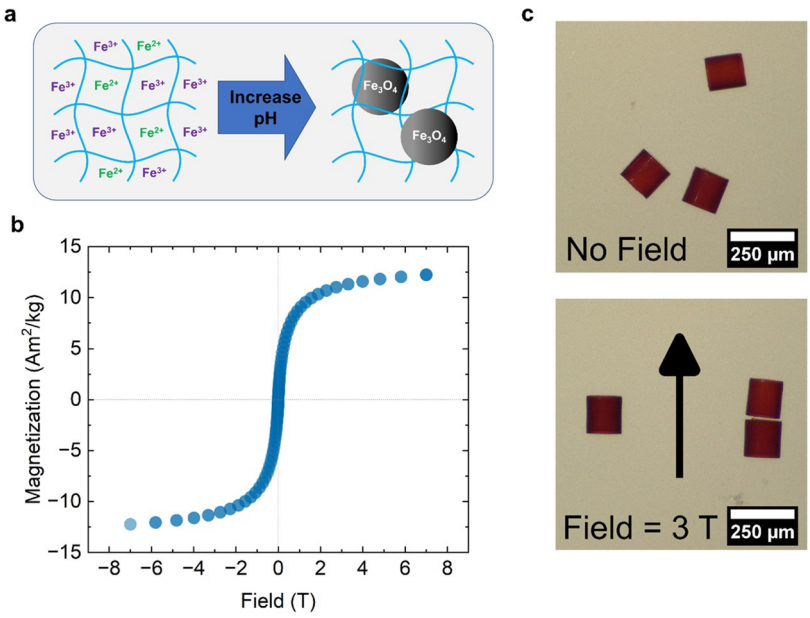

Figure 3. (a) Schematic description of the in situ coprecipitation process. A hydrogel swollen with an aqueous solution of iron cations is transferred into a bath of increased pH. The iron cations are not soluble in the basic solution, causing nucleation and growth of SPIONs throughout the hydrogel network. (b) Magnetization as a function of applied field for dried magnetogel microparticles taken at 300 K. (c) Effect of an applied magnetic field on the alignment of the GEMS is seen by inspecting the microparticles in pH 7 buffer before and after application of a 3 T magnetic field.

lithography.[21] The steps shown in Figure 2c,d were repeated to ensure that the hydrogel precursor had entirely filled the high-aspect-ratio interior of the PDMS molds. Then, the hydrogel precursor was cured within the molds by exposure to ultraviolet (UV) light (365 nm) under the flow of N_2 gas, which prevents the reaction of oxygen with the hydrogel precursor and photoinitiator (Figure 2e). Finally, to release the microparticles from the PDMS, the mold containing the cured microparticles was submerged in a 1:1 mixture of 0.5 mol/L NaOH in H_2O and isopropyl alcohol (IPA). The PEGDA/AA microparticles have the property that they swell when placed in basic solutions; as the mold was placed in the basic solution (0.5 mol/L NaOH and IPA), the swelling action of PEGDA/AA worked to push the microparticles out of the mold (Figure 2f). The microparticles were then collected via pipet and concentrated with centrifugal filters. Figure 2i shows dry microparticles deposited on a flat surface following fabrication.

In Situ Coprecipitation and Magnetic Properties. After soft lithography was used to create microparticles with the desired shape, the microparticles were further modified with SPION inclusions for magnetic functionality. In situ coprecipitation was used to grow SPIONs directly within the polymer network of the microparticles. During coprecipitation, the solubility of iron cations is reduced by increasing the pH of solution, causing nucleation and growth of SPIONs.[22−24] In situ coprecipitation is a modification of the standard coprecipitation process, where the nucleation and growth of nanoparticles occur in a porous medium or polymeric material and result in a nanoparticle-loaded material.[25−28] In situ coprecipitation has been used to prepare a variety of magnetic nanoparticle-loaded polymer particles, including PEGDA/AA hydrogel microparticles, and offers advantages compared to other techniques for magnetic modification of hydrogel microparticles.[29−31] Namely, the process is relatively simple compared to other types of magnetic nanoparticle synthesis, requiring cheap precursors and no specialized chemical apparatus.

Figure 3a shows a cartoon schematic of in situ coprecipitation. The hydrogel microparticles are first soaked in an aqueous solution of iron cations. Then, the swollen microparticles are transferred to a basic solution. As the basic solution diffuses through the polymer, the pH increases and drives the nucleation and growth of SPIONs via a reaction-diffusion process.[28] This process can produce different types of iron oxides, depending on the ratio of ferric (Fe^{3+}) and ferrous (Fe^{2+}) ions contained within the polymer network. Magnetite (Fe_3O_4) was the desired form of iron oxide, because of its large saturation magnetization at room temperature. Complete details of the in situ coprecipitation procedure are presented in the Supporting Information.

To better understand the magnetic properties of the GEMS, magnetometry was performed at room temperature (300 K). The mass magnetization of dry GEMS as a function of applied field shows a magnetization response with high susceptibility at low field, followed by saturation at high fields (Figure 3b). This response is characteristic of superparamagnetic nanoparticles. The mass magnetization of the composite reaches a value of 12.3 Am^2/kg at 7 T, which is 13.4% of the saturation magnetization of bulk magnetite.[32] This corresponds to a loading of ≈1 × 10^{11} SPIONs for each hollow cylinder GEMS microparticle (details in the Supporting Information).

For applications as MRI contrast agents, the GEMS will be subjected to strong magnetic fields. To investigate the mechanical response to magnetic fields, the GEMS were submerged in a pH 7 buffer within the well of a microscope slide and observed before and after being placed in the bore of a 3 T MRI scanner (Figure 3c). Before being put in the scanner, the GEMS microparticles have random orientations. After being placed in the bore and removed, the GEMS microparticles aligned with the direction of the applied magnetic field.

https://doi.org/10.1021/acssensors.3c01373
ACS Sens. 2024, 9, 42−51

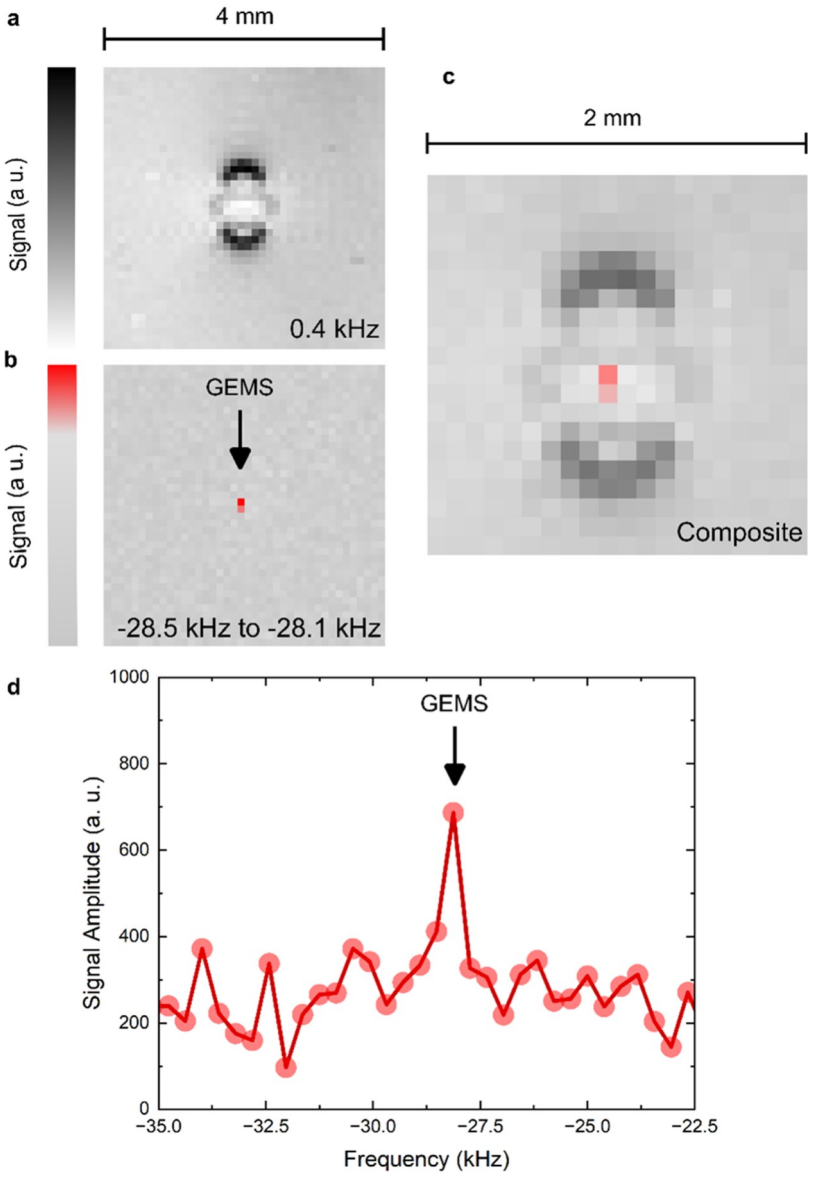

Figure 4. (a) Chemical shift image (CSI) of a 4 mm by 4 mm field of view containing a single GEMS at a frequency of offset of 0.4 kHz. Dipole artifacts from the magnetization of the magnetogel microparticle can be seen. (b) CSI of the same region of interest except the offset frequency range is −28.5 to −28.1 kHz. Two pixels in the center of the image show high-amplitude contributions from this range of the proton spectrum. (c) A composite image of (a) and (b) magnified to a 2 mm by 2 mm region of interest, showing the colocalization of the dipolar field artifacts and the high-amplitude region at −28.5 to −28.1 kHz. (d) Sum of the proton spectra for the two high-amplitude pixels showing a peak at −28.1 kHz from the GEMS frequency offset.

MULTISPECTRAL CONTRAST AND SMART SENSING

Demonstration of Multispectral Contrast from Single GEMS. To evaluate the multispectral contrast from the microparticles, a sample was prepared with GEMS embedded in agarose and loaded into a 9.4 T MRI. Figure 4 shows data taken from a single GEMS using a two-dimensional (2D) spin-echo chemical shift imaging (CSI) sequence, a spectroscopic MRI technique where a Larmor frequency proton spectrum is collected at each voxel. The in-plane resolution of the image is 100 μm × 100 μm, and the slice thickness, or the depth of the voxels, is 4 mm. The images in Figure 4a,b show a 4 mm by 4 mm region of interest, where the intensity of the images corresponds to the signal amplitude at specific frequencies. The regions of interest are the same for both images. A single GEMS is located at the center of the image, which generates the frequency-dependent contrast seen in Figure 4a,b. For each of the images, the zero frequency is defined by the maximum of the main water peak, which was estimated by looking at a voxel far from the GEMS. Figure 4a shows the amplitude of the spectrum for each voxel at a frequency offset of 0.4 kHz, which is close to the primary water peak. This image shows the signature of a magnetic dipole-based artifact, caused by the magnetization of the GEMS. Figure 4b shows the amplitude of the spectrum at offset frequencies ranging from −28.5 to −28.1 kHz. In this image, two voxels in the center of the field of view have higher signal amplitude than the rest of the image. The spectrum at these voxels, therefore, contains a high-amplitude component with a frequency of −28.1 to −28.5 kHz. Figure 4c shows a composite image formed from Figure 4a,b with a magnified field of view (2 mm). In this image, the high-

https://doi.org/10.1021/acssensors.3c01373
ACS Sens. 2024, 9, 42−51

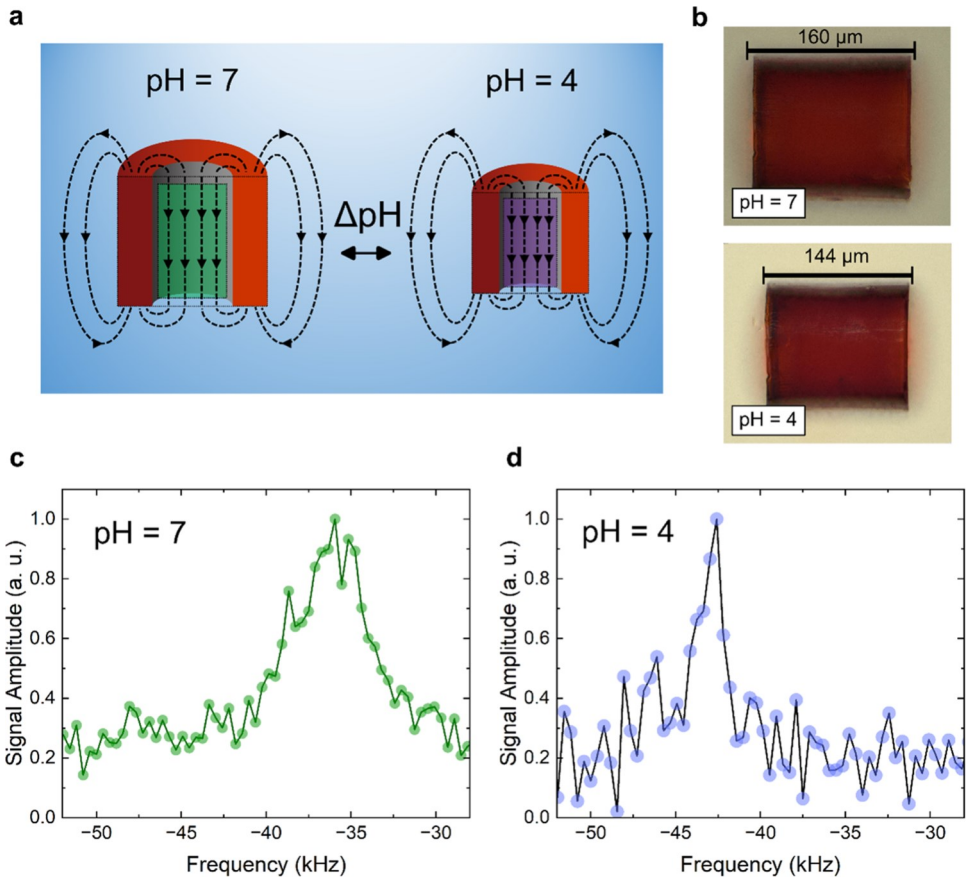

Figure 5. (a) Schematic showing the effect of pH-induced expansion and contraction on the magnetic field profile of the cylindrical shells. (b) Optical microscopy images of the GEMS in pH 7 and pH 4 buffer solution. The microparticles contract by a factor of $L_{pH\ 4}/L_{pH\ 7}$ = 0.9 when placed in pH 4 buffer. (c) Proton spectrum of single GEMS submerged in pH 7 buffer solution. (d) Proton spectrum of same GEMS except submerged in pH 4 buffer solution.

amplitude component around −28 kHz can be seen to be colocalized and centered within the dipolar field artifact caused by the GEMS. Figure 4d shows the sum of the proton spectra for the two voxels containing high-amplitude components at −28.1 to −28.5 kHz. The spectrum shows a clear peak compared to other frequencies. This colocalization implies that the resonance observed around −28 kHz is being created by the magnetic field within the cylindrical shell. The data shows that it is possible to localize the position of a single GEMS sensor to at least two voxels (i.e., 100 μm by 200 μm area) across a wide field of view (4 mm by 4 mm).

pH Sensing. The multispectral contrast from magnetogel GEMS can be used for MRI-addressable sensing by exploiting the response of environmentally sensitive, smart hydrogels. The magnetogel microparticles are made of a PEGDA/AA hydrogel, which undergoes reversible shape change in response to pH (Figure 5a). Specifically, the hydrogel contracts under acidic conditions and expands under neutral or basic pH. Figure 5b shows optical images of the GEMS microparticles in pH 7 and 4 buffers. When placed in pH 4 buffer, the GEMS change their length by a factor of $L_{pH\ 4}/L_{pH\ 7}$ = 0.9. This pH-induced volume change will affect the frequency offset of the GEMS. The decrease in hydrogel volume has the effect of increasing the magnetization per unit volume since the number of SPIONs remains the same throughout contraction. The increased magnetization of the GEMS works to further reduce the net magnetic field inside of the cylinder, which is a sum of the field from the GEMS and the B_0 field, causing the frequency offset to shift further away from the primary water peak. The decrease in the volume also decreases the volume of the cylindrical shell interior. Fewer protons can occupy the volume inside the hollow cylinder, meaning that contraction reduces the signal from a single device.

To explore the sensing capabilities of the GEMS, we interrogated individual microparticles using 9.4 T MRI (details in "Materials and methods" section in the Supporting Information). Figure 5c shows the normalized proton spectrum for a single GEMS in pH 7 buffer solution. The spectrum shows a frequency offset of −36 kHz. After this measurement, the wells containing the buffer solution and individual GEMS were emptied and replaced with a pH 4 buffer solution. After the buffers were changed, the same individual GEMS was measured again. Figure 5d shows the normalized proton spectrum at pH 4 with a peak that shifted to −43 kHz. The decreased frequency offset corresponds to an increase in the effective magnetization per unit volume of the contracted cylinder.

The relationship between the volume of a sensor and the corresponding frequency shift can be understood by recasting eq 1 as the changed offset frequency, f'_{offset}, due to an isotropic volume change, $V' = \alpha V$,

https://doi.org/10.1021/acssensors.3c01373
ACS Sens. 2024, 9, 42−51

$$f'_{\text{offset}} = \mu_0 \gamma \frac{m}{V'} \left(\frac{L}{\sqrt{L^2 + (2\rho + t)^2}} - \frac{L}{\sqrt{L^2 + (2\rho - t)^2}} \right) \propto \frac{1}{\alpha} f_{\text{offset}} \quad (2)$$

where m is the magnetic moment of the cylinder and α is a scaling factor associated with volume change. For an isotropic expansion or contraction, the geometric parameters of the cylinder (L, 2ρ, t) are all rescaled by the same factor, and so their contribution to the frequency offset remains constant. The magnetic moment, m, remains constant since the number of SPIONs within the hydrogel matrix stays the same throughout an expansion or contraction process. The change in the frequency therefore scales simply as the inverse of the volume scaling factor, $1/\alpha$.

The scaling can be used to estimate the expected change in offset frequency for the GEMS at pH 4 and pH 7 by using the optical images in Figure 5b. The scaling factor, α, is proportional to the fractional length change between expanded and contracted states raised to the third power, $\alpha \propto (L_{\text{pH 4}}/L_{\text{pH 7}})^3 \approx 0.73$. Rescaling the frequency offset at pH 7 (−36 kHz) by the inverse, $1/\alpha$, predicts a frequency offset of −49 kHz for pH 4 for an ideal isotropic expansion. The actual frequency change measured by MRI in these experiments is not as large and could be caused by several factors such as variation in swelling from microparticle to microparticle or imperfect alignment of the GEMS with respect to the MRI field, which may be due to some rotational hindrance within the wells used for the experiment. It is also possible that some trace of the pH 7 buffer solution remained in the wells after the first experiments, increasing the net pH in the wells after they had been filled with pH 4 buffer solution.

The relationship expressed in eq 2 indicates that the sensitivity of GEMS could be tuned by adjusting the polymeric properties of the magnetogel. The magnitude of the smart swelling response of the composite, and the corresponding shift in frequency offset, can be adjusted via the cross-linking density or the molecular weight of the monomers within the polymer network.

DISCUSSION

This work shows that soft lithographic approaches to GEMS fabrication can produce microparticles with the requisite shape and magnetic functionality to generate multispectral contrast. The fabrication scheme presented here offers several advantages over previous routes for GEMS production, which relied on thin-film lithography techniques.[6−12] Soft lithography is performed outside of a cleanroom environment except for the initial fabrication of the master mold. This significantly reduces the infrastructure needed to fabricate these devices. Soft lithography can also be performed with a small set of relatively cheap materials. The addition of magnetic functionality is realized by growing magnetic SPIONs throughout GEMS using in situ coprecipitation. Compared to thin-film techniques, in situ coprecipitation is a cheaper way to deposit magnetic material compared with high-vacuum evaporation or sputtering methods.

The magnetization of the GEMS can be tuned by performing different numbers of SPION growth steps, so there exists a straightforward pathway for producing sets of microparticles with different frequency offsets or colors for multiplexed labeling and sensing. Also, since the magnetic functionality of the magnetogel arises from an ensemble of superparamagnetic nanoparticles, the GEMS display an overall superparamagnetic response to magnetic fields. It has been suggested that magnetic particles with zero magnetization remnant states are ideal for biological applications because they will not interact via remnant dipole moments.[33] The GEMS have minimal remnant magnetization due to their superparamagnetic property (Figure 3b) and, therefore, do not aggregate from magnetic dipole−dipole interactions in zero field. It should be noted, however, that the strong applied magnetic fields into which the GEMS are placed will still induce net magnetization in superparamagnetic GEMS, which may drive aggregation and chaining.

The magnetogel GEMS have multispectral properties that may be useful for applications in labeling and tracking. In these experiments, it was possible to localize a signal from a single GEMS to an area that was 800-fold smaller than the overall field of view. Specifically, it was possible to locate a GEMS with a swollen volume of ≈160 μm over a field of view of 4 mm by 4 mm, with a slice depth of 4 mm. In principle, however, it should be possible to identify a single GEMS over even larger three-dimensional volumes. The spectral signal used to localize the GEMS occurred at a frequency of about −28 kHz, which is well separated in frequency space from the background at the primary water peak. A shift of −28 kHz corresponds to a shift of −70 ppm at 9.4 T, which is larger than chemical shifts of naturally occurring hydrocarbons or organic compounds.[34] The spatial sensitivity of the GEMS suggests that they may be useful for tagging microscale targets in bioenvironments or fluid-filled materials.

Further optimization of both soft lithography and magnetic functionalization of GEMS can lead to improved performance. It should be possible to miniaturize the devices further using molding techniques in order to produce cellular-scale MRI reporters since soft lithography can replicate patterns down to submicron levels.[14] Also, the magnitude of the frequency shift may be increased by refining the in situ coprecipitation to produce devices with a higher magnetization. For example, hydrogel microparticles with a mass magnetization of 42 Am^2/kg have been created using in situ coprecipitation.[31] GEMS devices made with this magnetization could produce frequency offsets 5× higher than the devices reported here. The in situ coprecipitation and fabrication process can also be improved to produce GEMS with greater uniformity in magnetization. For these first experiments, sensors from the same batch of GEMS exhibited a range of frequency offsets (Supporting Information). The variation in magnetization may arise from nonuniform evaporation of acrylic acid across the mold prior to UV curing of the hydrogel. The density of acrylic acid affects the final magnetization of the microparticles and the amount by which those GEMS shrink or swell under different pH conditions; therefore, the evaporation could be better controlled in the future to produce GEMS with uniform magnetic properties.

Compared to previous GEMS made in a cleanroom environment, the magnetogel cylinders described here have inherent benefits but also disadvantages. As already mentioned, the fabrication scheme is simplified compared with those used in cleanroom environments. An additional advantage is that the sensing modality here may offer increased sensitivity over previous GEMS, which relied on hydrogel expansion between two micropatterned ferromagnetic disks. The sensitivity for these "double-disk" sensors scales with the change in distance

https://doi.org/10.1021/acssensors.3c01373
ACS Sens. 2024, 9, 42−51

between the disks and is therefore proportional to a length change in one dimension.[9] The magnetogel cylinders, however, have a sensitivity that scales with a change in their overall volume, which is proportional to their cubed length.

The primary disadvantage of this process, when compared to thin-film fabrication, is a loss in precision microengineering. Tools in a cleanroom environment regularly produce devices with precision on the order of single nanometers, and so will still be favored for situations where devices require resolution on ultrasmall length scales. Still, the advantages conferred by the relative simplicity of the GEMS described here justify continued research into soft lithographic approaches for GEMS production.

In the future, we plan to explore the potential of these GEMS as biosensors. We note, however, that the GEMS need further development before they are ready for biosensing applications. Additional studies are needed to determine how the sensors operate in complex bioenvironments and reduction in the size of the sensors will be needed to probe cellular length scales. Still, in their current form, GEMS have properties that lend themselves to biological applications. The swelling response of PEGDA-based hydrogels operates across a range of biologically relevant pH values, creating opportunities for sensing biochemical processes.[35] Additionally, the GEMS described here were fabricated from a poly(ethylene glycol) (PEG)-based hydrogel, and PEG is a biocompatible polymer used for a variety of biomedical applications.[36,37] At their current size, GEMS might be used as gastrointestinal pH sensors. With further miniaturization, they may also be useful for probing acidification in lysosomes[38,39] or acid−base homeostasis in tumor microenvironments.[40,41] The magnetogel GEMS can provide sensing possibilities beyond pH, as well, by using hydrogels that have different smart functionalities.

CONCLUSIONS

This work outlines an alternative method for fabricating multispectral GEMS by using a soft lithography approach. Previous techniques for fabricating these types of contrast agents have used advanced thin-film lithography techniques and a cleanroom environment, which require substantial infrastructure and expertise. Soft lithography, on the other hand, uses a small set of relatively inexpensive materials and can be performed in a standard laboratory environment once an initial microfabricated template is produced. Moreover, magnetic functionality is added to the GEMS through in situ coprecipitation, which uses simple chemistry and cheap chemical precursors. The GEMS are made of a magnetogel composite and can have frequency shifts well beyond standard chemical shifts for hydrocarbons or common organic molecules, providing pathways for unambiguous identification and localization with MRI. The magnetogel composites can also be fabricated using smart hydrogels, which change their geometry and corresponding frequency in response to environmental stimuli. An example of pH sensing is described, where the sensors display a detectable shift in frequency offset as the pH is changed from 7 to 4. Taken together, these results show that soft lithography can be used to produce GEMS in a manner that is less expensive and requires less infrastructure than advanced thin-film lithography while at the same time retaining the key functionalities of multispectral contrast agents.

EXPERIMENTAL SECTION

This section contains essential experimental procedures used in the manuscript. A more detailed description of all materials and methods is included in the Supporting Information.

Fabrication of Silicon Master Molds. Silicon master molds were fabricated by using photolithography and deep reactive ion etching. Details are described in the Supporting Information.

Fabrication of Silicon Wells for pH Experiments. Silicon wells used in pH sensing experiments were fabricated by using photolithography and deep reactive ion etching. The rectangular wells had dimensions of 180 μm wide, 180 μm long, and 175 μm deep. Full details are given in the Supporting Information.

Creation of Elastomer Molds. The PDMS precursor was first prepared by mixing the Sylgard 184 base and curing agent together in a 10:1 mixture of base to curing agent. Then, the liquid PDMS precursor was poured on top of a micropatterned Si mold, degassed using a bell har and diaphragm pump to remove bubbles, and heated at 110 °C for 70 min. After heating, the wafer was cooled to room temperature, and the elastomer could be peeled away from the silicon. Additional details and pictures of the process are provided in the Supporting Information.

Fabrication of Hydrogel Microparticles. Cylindrical shell-shaped hydrogel microparticles were fabricated using micromolding techniques with PDMS templates. The PDMS templates were filled with liquid hydrogel precursor by using discontinuous dewetting. Then, the precursor was cured with ultraviolet light and the particles were removed from the PDMS. More details are included in the Supporting Information.

In Situ Coprecipitation. For in situ coprecipitation, we followed a modified version of the procedure described by Suh et al. for growing magnetite nanoparticles in hydrogel microparticles made of PEGDA/AA.[31] Complete details are described in the Supporting Information.

Magnetic Resonance Imaging. All MRI experiments were performed with a Bruker 9.4 T MRI scanner. The sensors were probed with a 2D spin-echo chemical shift imaging (CSI) sequence, a spectroscopic technique used to acquire a proton Larmor frequency spectrum at each voxel. The repetition time (TR) was 150 ms, and the echo time (TE) was 1.6 ms. For the localization experiments with GEMS embedded in a Petri dish filled with agarose, the voxel size was 0.1 mm × 0.1 mm × 4 mm depth. For the pH sensing experiments, the voxel size was 0.1 mm × 0.1 mm laterally but extended vertically through the full depth of the wells, meaning the slice thickness was effectively determined by the depth of the wells, which were 175 μm deep.

Magnetometry. Magnetization as a function of the applied field was collected using a Quantum Design MPMS3 magnetometer. Details are included in the Supporting Information.

Magnetic Field Simulations. Simulations of the magnetic field surrounding cylindrical shell structures were performed using COMSOL Multiphysics 5.4. The magnetic field from simulations was evaluated with a grid generated by a custom Python code. Details are included in the Supporting Information.

DISCLAIMER

Any mention of commercial products is intended solely for fully detailing experiments; it does not imply recommendation or endorsement by the National Institute of Standards and Technology (NIST).

ASSOCIATED CONTENT

* Supporting Information

The Supporting Information is available free of charge at https://pubs.acs.org/doi/10.1021/acssensors.3c01373.

Additional details on materials and methods, microfabrication procedures, magnetometry, magnetic field simulations, pictures of PDMS mold preparation,

https://doi.org/10.1021/acssensors.3c01373
ACS Sens. 2024, 9, 42−51

experimental details for pH sensing experiments, an estimation of SPION density in microparticles, and measurements of the stability of the microparticles' magnetic properties (PDF)

AUTHOR INFORMATION

Corresponding Authors

Samuel D. Oberdick − *Department of Physics, University of Colorado, Boulder, Colorado 80309, United States; National Institute of Standards and Technology, Boulder, Colorado 80305, United States;* orcid.org/0000-0003-4214-7492; Email: samuel.oberdick@nist.gov

Gary Zabow − *National Institute of Standards and Technology, Boulder, Colorado 80305, United States*; Email: gary.zabow@nist.gov

Authors

Stephen J. Dodd − *Laboratory of Functional and Molecular Imaging, NINDS, National Institutes of Health, Bethesda, Maryland 20892, United States*

Alan P. Koretsky − *Laboratory of Functional and Molecular Imaging, NINDS, National Institutes of Health, Bethesda, Maryland 20892, United States*

Complete contact information is available at: https://pubs.acs.org/10.1021/acssensors.3c01373

Notes

The authors declare no competing financial interest.

ACKNOWLEDGMENTS

This research was funded by NIST (http://ror.org/05xpvk416), the National Science Foundation (NSF) (https://ror.org/021nxhr62), the National Academies of Sciences, Engineering and Medicine (http://ror.org/02eq2w707), and the Intramural Research Program of the National Institutes of Neurological Disorders and Stroke (https://ror.org/01s5ya894) at the National Institutes of Health (https://ror.org/01cwqze88). S.D.O. (https://orcid.org/0000-0003-4214-7492) was supported through PREP agreement no. 70NANB18H006 between NIST and the University of Colorado, Boulder (http://ror.org/02ttsq026) and a National Research Council (NRC) Postdoctoral Fellowship from the National Academies of Sciences, Engineering and Medicine (http://ror.org/02eq2w707). S.D.O. acknowledges support from the NSF (https://ror.org/021nxhr62) through NSF-CBET award no. 2038046. Research performed at the National Institutes for Neurological Disorders and Stroke (https://ror.org/01s5ya894) was supported by Intramural NINDS Z01-NS003047.

REFERENCES

(1) Carregal-Romero, S.; Caballero-Díaz, E.; Beqa, L.; Abdelmonem, A. M.; Ochs, M.; Huhn, D.; Suau, B. S.; Valcarcel, M.; Parak, W. J. Multiplexed Sensing and Imaging with Colloidal Nano- and Microparticles. *Annu. Rev. Anal. Chem.* 2013, *6* (1), 53−81.

(2) Han, X.; Xu, K.; Taratula, O.; Farsad, K. Applications of Nanoparticles in Biomedical Imaging. *Nanoscale* 2019, *11* (3), 799−819.

(3) Gao, Z.; Ma, T.; Zhao, E.; Docter, D.; Yang, W.; Stauber, R. H.; Gao, M. Small Is Smarter: Nano MRI Contrast Agents−Advantages and Recent Achievements. *Small* 2016, *12* (5), 556−576.

(4) Fu, S.; Cai, Z.; Ai, H. Stimulus-Responsive Nanoparticle Magnetic Resonance Imaging Contrast Agents: Design Considerations and Applications. *Adv. Healthcare Mater.* 2021, *10* (5), No. 2001091.

(5) van Moolenbroek, G. T.; Patino, T.; Llop, J.; Sánchez, S. Engineering Intelligent Nanosystems for Enhanced Medical Imaging. *Adv. Intell. Syst.* 2020, *2* (10), No. 2000087.

(6) Zabow, G.; Dodd, S.; Moreland, J.; Koretsky, A. Micro-Engineered Local Field Control for High-Sensitivity Multispectral MRI. *Nature* 2008, *453* (7198), 1058−1063.

(7) Zabow, G.; Dodd, S. J.; Moreland, J.; Koretsky, A. P. The Fabrication of Uniform Cylindrical Nanoshells and Their Use as Spectrally Tunable MRI Contrast Agents. *Nanotechnology* 2009, *20* (38), No. 385301.

(8) Zabow, G.; Dodd, S. J.; Koretsky, A. P. Ellipsoidal Microcavities: Electromagnetic Properties, Fabrication, and Use as Multispectral MRI Agents. *Small* 2014, *10* (10), 1902−1907.

(9) Zabow, G.; Dodd, S. J.; Koretsky, A. P. Shape-Changing Magnetic Assemblies as High-Sensitivity NMR-Readable Nanoprobes. *Nature* 2015, *520* (7545), 73−77.

(10) Wang, X.; Wang, C.; Anderson, S.; Zhang, X. Microfabricated Iron Oxide Particles for Tunable, Multispectral Magnetic Resonance Imaging. *Mater. Lett.* 2013, *110*, 122−126.

(11) Wang, X.; Zhang, X.; Anderson, S. W. A Novel Contrast Agent for Multispectral Magnetic Resonance Imaging. *Sensors* 2010, 1305−1308.

(12) Wang, C.; Wang, X.; Anderson, S. W.; Zhang, X. Biocompatible, Micro- and Nano-Fabricated Magnetic Cylinders for Potential Use as Contrast Agents for Magnetic Resonance Imaging. *Sens. Actuators, B* 2014, *196*, 670−675.

(13) Xia, Y.; Whitesides, G. M. Soft Lithography. *Angew. Chem., Int. Ed.* 1998, *37* (5), 550−575.

(14) Qin, D.; Xia, Y.; Whitesides, G. M. Soft Lithography for Micro- and Nanoscale Patterning. *Nat. Protoc.* 2010, *5* (3), 491−502.

(15) Rolland, J. P.; Maynor, B. W.; Euliss, L. E.; Exner, A. E.; Denison, G. M.; DeSimone, J. M. Direct Fabrication and Harvesting of Monodisperse, Shape-Specific Nanobiomaterials. *J. Am. Chem. Soc.* 2005, *127* (28), 10096−10100.

(16) Merkel, T. J.; Herlihy, K. P.; Nunes, J.; Orgel, R. M.; Rolland, J. P.; DeSimone, J. M. Scalable, Shape-Specific, Top-Down Fabrication Methods for the Synthesis of Engineered Colloidal Particles. *Langmuir* 2010, *26* (16), 13086−13096.

(17) Oberdick, S. D.; Zabow, G. Patterned Surface Energy in Elastomeric Molds as a Generalized Approach to Polymer Particle Fabrication. *ACS Appl. Polym. Mater.* 2020, *2* (2), 846−852.

(18) Guan, J.; Chakrapani, A.; Hansford, D. J. Polymer Microparticles Fabricated by Soft Lithography. *Chem. Mater.* 2005, *17* (25), 6227−6229.

(19) Guan, J.; Ferrell, N.; James Lee, L.; Hansford, D. J. Fabrication of Polymeric Microparticles for Drug Delivery by Soft Lithography. *Biomaterials* 2006, *27* (21), 4034−4041.

(20) Jackman, R. J.; Duffy, D. C.; Ostuni, E.; Willmore, N. D.; Whitesides, G. M. Fabricating Large Arrays of Microwells with Arbitrary Dimensions and Filling Them Using Discontinuous Dewetting. *Anal. Chem.* 1998, *70* (11), 2280−2287.

(21) Kim, H. U.; Roh, Y. H.; Mun, S. J.; Bong, K. W. Discontinuous Dewetting in a Degassed Mold for Fabrication of Homogeneous Polymeric Microparticles. *ACS Appl. Mater. Interfaces* 2020, *12* (47), 53318−53327.

(22) Massart, R. Preparation of Aqueous Magnetic Liquids in Alkaline and Acidic Media. *IEEE Trans. Magn.* 1981, *17* (2), 1247−1248.

(23) Ahn, T.; Kim, J. H.; Yang, H.-M.; Lee, J. W.; Kim, J.-D. Formation Pathways of Magnetite Nanoparticles by Coprecipitation Method. *J. Phys. Chem. C* 2012, *116* (10), 6069−6076.

(24) Qiao, R.; Yang, C.; Gao, M. Superparamagnetic Iron Oxide Nanoparticles: From Preparations to in Vivo MRI Applications. *J. Mater. Chem.* 2009, *19* (35), 6274−6293.

(25) Helminger, M.; Wu, B.; Kollmann, T.; Benke, D.; Schwahn, D.; Pipich, V.; Faivre, D.; Zahn, D.; Cölfen, H. Synthesis and

Characterization of Gelatin-Based Magnetic Hydrogels. *Adv. Funct. Mater.* 2014, *24* (21), 3187−3196.
(26) Li, Y.; Huang, G.; Zhang, X.; Li, B.; Chen, Y.; Lu, T.; Lu, T. J.; Xu, F. Magnetic Hydrogels and Their Potential Biomedical Applications. *Adv. Funct. Mater.* 2013, *23* (6), 660−672.
(27) Starodubtsev, S. G.; Saenko, E. V.; Dokukin, M. E.; Aksenov, V.; Klechkovskaya, V. V.; Zanaveskina, I. S.; Khokhlov, A. R. Formation of Magnetite Nanoparticles in Poly(Acrylamide) Gels. *J. Phys.: Condens.Matter* 2005, *17* (10), 1471−1480.
(28) Oberdick, S. D.; Russek, S. E.; Poorman, M. E.; Zabow, G. Observation of Iron Oxide Nanoparticle Synthesis in Magnetogels Using Magnetic Resonance Imaging. *Soft Matter* 2020, *16* (45), 10244−10251.
(29) Ugelstad, J.; Berge, A.; Ellingsen, T.; Schmid, R.; Nilsen, T.-N.; Mørk, P. C.; Stenstad, P.; Hornes, E.; Olsvik, Ø. Preparation and Application of New Monosized Polymer Particles. *Prog. Polym. Sci.* 1992, *17* (1), 87−161.
(30) Huang, J.; Wan, S.; Guo, M.; Yan, H. Preparation of Narrow or Mono-Disperse Crosslinked Poly((Meth)Acrylic Acid)/Iron Oxide Magnetic Microspheres. *J. Mater. Chem.* 2006, *16* (46), 4535−4541.
(31) Suh, S. K.; Yuet, K.; Hwang, D. K.; Bong, K. W.; Doyle, P. S.; Hatton, T. A. Synthesis of Nonspherical Superparamagnetic Particles: In Situ Coprecipitation of Magnetic Nanoparticles in Microgels Prepared by Stop-Flow Lithography. *J. Am. Chem. Soc.* 2012, *134* (17), 7337−7343.
(32) Cullity, B. D.; Graham, C. D. *Introduction to Magnetic Materials*; John Wiley & Sons, 2011.
(33) Vemulkar, T.; Mansell, R.; Petit, D. C. M. C.; Cowburn, R. P.; Lesniak, M. S. Highly Tunable Perpendicularly Magnetized Synthetic Antiferromagnets for Biotechnology Applications. *Appl. Phys. Lett.* 2015, *107* (1), No. 012403.
(34) Carrington, A.; McLachlan, A. D. *Introduction to Magnetic Resonance: With Applications to Chemistry and Chemical Physics*; Chapman and Hall, 1979.
(35) Cavallo, A.; Madaghiele, M.; Masullo, U.; Lionetto, M. G.; Sannino, A. Photo-Crosslinked Poly(Ethylene Glycol) Diacrylate (PEGDA) Hydrogels from Low Molecular Weight Prepolymer: Swelling and Permeation Studies. *J. Appl. Polym. Sci.* 2017, *134* (2), No. 44380, DOI: 10.1002/app.44380.
(36) Zalipsky, S.; Harris, J. M. Introduction to Chemistry and Biological Applications of Poly(Ethylene Glycol). In *Poly(ethylene glycol)*; ACS Symposium Series; American Chemical Society, 1997; Vol. *680*, pp 1−13.
(37) Otsuka, H.; Nagasaki, Y.; Kataoka, K. PEGylated Nanoparticles for Biological and Pharmaceutical Applications. *Adv. Drug Delivery Rev.* 2003, *55* (3), 403−419.
(38) Mindell, J. A. Lysosomal Acidification Mechanisms. *Annu. Rev. Physiol.* 2012, *74* (1), 69−86.
(39) Canton, J.; Grinstein, S. Measuring Lysosomal pH by Fluorescence Microscopy. In *Methods in Cell Biology*; Platt, F.; Platt, N., Eds.; Lysosomes and Lysosomal Diseases; Academic Press, 2015; Chapter 5, Vol. *126*, pp 85−99.
(40) Tannock, I. F.; Rotin, D. Acid pH in Tumors and Its Potential for Therapeutic Exploitation. *Cancer Res.* 1989, *49* (16), 4373−4384.
(41) Zhang, X.; Lin, Y.; Gillies, R. J. Tumor pH and Its Measurement. *J. Nucl. Med.* 2010, *51* (8), 1167−1170.

https://doi.org/10.1021/acssensors.3c01373
ACS Sens. 2024, 9, 42−51